MATERIALS SCIENCE

Controlling ice formation on gradient wettability surface for high-performance bioinspired materials

Nifang Zhao*, Meng Li*, Huaxin Gong, Hao Bai†

Ice-templating holds promise to become a powerful technique to construct high-performance bioinspired materials. Both ice nucleation and growth during the freezing process are crucial for the final architecture of the ice-templated material. However, effective ways to control these two very important factors are still lacking. Here, we demonstrate that successive ice nucleation and preferential growth can be realized by introducing a wettability gradient on a cold finger. A bulk porous material with a long-range lamellar pattern was obtained using a linear gradient, yielding a high-performance, bulk nacre-mimetic composite with excellent strength and toughness after infiltration. In addition, cross-aligned and circular lamellar structures can be obtained by freeze-casting on surfaces modified with bilayer linear gradient and radial gradient, respectively, which are impossible to realize with conventional freeze-casting techniques. Our study highlights the potential of harnessing the rich designability of surface wettability patterns to build high-performance bulk materials with bioinspired complex architectures.

INTRODUCTION

Many biological materials, such as nacre, bone, and teeth, have long served as a source of inspiration for developing high-performance structural materials (*1*–*3*). With a very limited selection of relatively weak constituents, these biological materials realize outstanding mechanical properties by building sophisticated hierarchical architectures ranging from nano/micro- to macroscopic levels (*4*). A prime example is nacre, which achieves both excellent strength and toughness by assembling 95 volume percent (volume %) of brittle $CaCO_3$ platelets and 5 volume % of biopolymer into a "brick-and-mortar" architecture (*5*). During the past decade, various methods have been applied to develop nacre-mimetic composites (*6*), including vacuum filtration (*7*), layer-by-layer assembly (*8*–*10*), freeze-casting (*11*–*13*), mineralization (*14*), co-extruding (*15*), and three-dimensional printing (*16*). Specifically, freeze-casting (or ice-templating) holds promise to become a powerful technique with a balance between precise architectural control, easy scalability, versatility, and low cost, which are all important for the practical application of high-performance nacre-mimetic composites.

With its outstanding versatility, freeze-casting has been applied to assemble various building blocks, including ceramics (*17*, *18*), polymers (*19*), carbon nanotubes (*20*), graphene (*21*), and boron nitride (*22*), into bulk materials with nacre-mimetic lamellar layers. In a typical freeze-casting process, the ice crystals nucleate on a cold surface and grow with a preferred direction along the temperature gradient. Obviously, controlling ice nucleation and growth is crucial, as the architecture of the resulting porous material simply replicates the ice crystal morphology. In this context, parameters such as temperature gradient direction (*23*–*25*), additive type and concentration (*26*, *27*), and magnetic field (*28*, *29*) have been revealed to have a profound impact on the final architecture. The properties of the cold surface (two-dimensional) also require careful design to control the architecture of the ice-templated material (three-dimensional) (*26*, *30*).

State Key Laboratory of Chemical Engineering, College of Chemical and Biological Engineering, Zhejiang University, Hangzhou 310027, China.
*These authors contributed equally to this work.
†Corresponding author. Email: hbai@zju.edu.cn

Here, we report our successful attempt in this direction focusing on the role of surface wettability. Specifically, we are able to control ice nucleation and growth on a cold surface by introducing a wettability gradient. An aqueous slurry containing hydroxyapatite (HA) particles is used in the current study as a proof of concept. The ice crystals nucleate successively from the hydrophilic to hydrophobic region and align perpendicularly to the wettability gradient, yielding a bulk porous material with a long-range lamellar pattern (>10 cm, limited only by size of the cooling stage). Subsequent infiltration of this porous scaffold generates a high-performance, bulk nacre-mimetic composite with excellent strength and toughness. In addition, cross-aligned and circular lamellar structures can be obtained by freeze-casting on surfaces modified with bilayer linear wettability gradient and radial wettability gradient, respectively, which are impossible to realize with conventional freeze-casting techniques. Our study highlights the possibility of harnessing the rich designability of surface wettability patterns for the fabrication of bulk materials with biomimetic sophisticated architectures.

RESULTS AND DISCUSSION

Comparison of freeze-casting processes on surfaces with various wettability

Figure 1 compares freeze-casting processes on surfaces with various wettability (i.e., homogeneously hydrophilic, homogeneously hydrophobic, and gradient) and the resulting microstructures, respectively. In all three cases, the same HA slurry with 20 volume % of HA particles, 1 weight % (wt %) of Darvan 811 as dispersant, 1 wt % of poly(ethylene glycol) as lubricant, and 2 wt % of Aquazol as binder was used. Although HA was used as a proof of concept to study the effect of surface wettability in detail, our technique can also be applied to assemble other colloids. Figure 1A shows a traditional freeze-casting process (*11*, *12*), where the slurry is in direct contact with an unmodified, homogeneously hydrophilic copper substrate. Upon cooling, a vertical temperature gradient (ΔT) is generated, guiding the ice crystals to grow preferentially from the bottom to the top. As the cold copper substrate is homogeneously hydrophilic with a water contact angle of ~20°, ice nucleation happens simultaneously all over the surface. In addition, as there is no

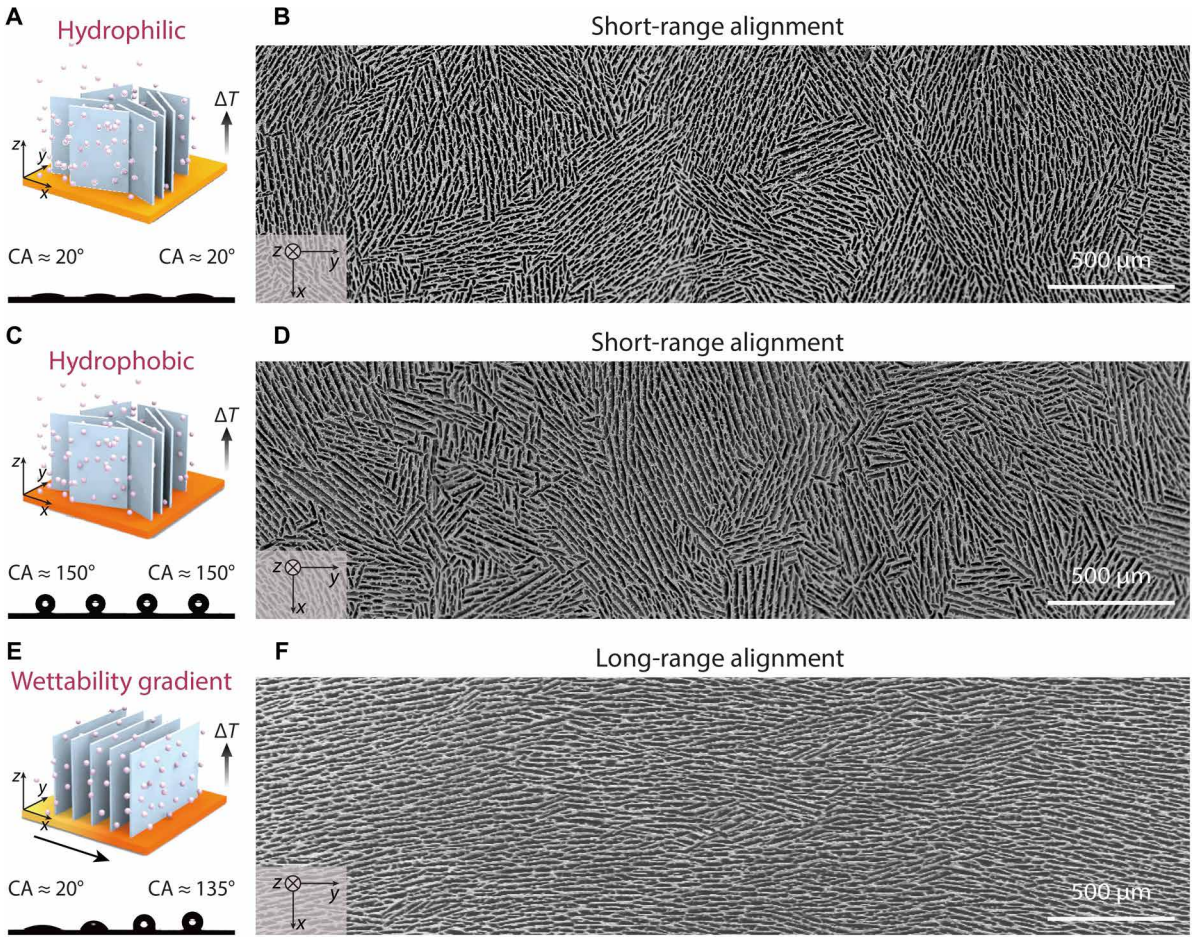

Fig. 1. Freeze-casting technique using copper surfaces with different wettability and the resulting scaffolds. SEM images were taken from the cross section of 1-cm height parallel to the cold surface. (**A** to **D**) When freezing on the homogeneously hydrophilic and hydrophobic copper substrates, the ice crystals nucleate simultaneously over the surfaces and grow without a preferred direction, resulting in a short-range lamellar structure that contains various randomly oriented domains. (**E** and **F**) When freezing on a copper surface with a linear wettability gradient, the ice crystals align perpendicular to the gradient, resulting in a long-range lamellar structure with only a single domain.

preferred ice growth direction in the horizontal plane, only submillimeter lamellar domains can be obtained corresponding to various orientations of ice crystals. This is clearly observed in the horizontal cross section (*xy* plane) of the resulting scaffold after sublimation, as shown by the scanning electron microscopic (SEM) image in Fig. 1B.

It is well known that ice crystals nucleate more easily on a hydrophilic surface than a hydrophobic one because of the much lower energy barrier, which has been intensively studied in the anti-icing property of superhydrophobic surfaces (*31*, *32*). However, applying this principle to control ice orientation and therefore the architecture of the resulting material has rarely been attempted.

Our first attempt was to repeat the same freeze-casting procedure on a hydrophobic copper surface homogeneously modified with 1*H*,1*H*,2*H*,2*H*-perfluorooctyltriethoxysilane (POTS). The water contact angle is ~150° all over the surface (Fig. 1C). Although the overall ice nucleation rate is delayed, it does not vary for different regions as the surface is homogeneous. As a result, the ice crystals still nucleate randomly over the surface without a preferred orientation in the horizontal plane, just as on a hydrophilic surface. A similar short-range alignment is observed in the horizontal cross section of the resulting scaffold, as demonstrated by the SEM image in Fig. 1D. This suggests that homogeneous modification of surface wettability is inadequate to change the orientation of ice crystals.

Following the same principle, we attempted to design more complex wettability patterns for freeze-casting. As a proof of concept, we modified the copper surface with POTS by programmed dip-coating (fig. S1), yielding a linear wettability gradient with the water contact angle increasing from ~20° to ~135° (Fig. 1E). The wettability changes over a length of 12 mm. After performing the same freeze-casting procedure, we obtained a scaffold with long-range aligned lamellar layers (SEM in Fig. 1F), drastically different from those obtained from the previous two homogeneous surfaces. This indicates that the orientations of ice crystals are all shifted to the perpendicular direction of the wettability gradient (Fig. 1E). The SEM images taken from the cross section both perpendicular to the cold surface (fig. S2) and parallel to the cold surface (fig. S3) show that aligned lamellar layers are consistent throughout the observed area. We have achieved similar long-range lamellar structure on a glass substrate modified with a similar wettability gradient (fig. S4). This further suggests that it is the surface wettability rather than the type of surface material that determines the orientation of ice crystals.

We note that a similar monodomain lamellar structure can be obtained by the bidirectional freezing (*23*, *24*, *33*) or freezing-under-flow

(*34*) techniques. However, our current approach overcomes the size limitation resulting from the polydimethylsiloxane wedge length or mold width. We highlight the possibility of harnessing the rich designability of surface wettability patterns to generate more complex bioinspired architectures, which have remained challenging for many years with conventional freeze-casting techniques (*13*). This is confirmed by the cross-aligned and circular lamellar structures obtained by freeze-casting on copper surfaces with bilayer linear wettability gradient and radial wettability gradient, respectively. A more detailed discussion can be found later in the text.

Observation of the freezing process

To probe the mechanism, we observed the freezing process in situ under an optical microscope (Fig. 2A). The setup is illustrated in fig. S5. A Teflon mold (12 mm by 12 mm by 1 mm) was sealed to the copper substrate with a linear wettability gradient from ~20° to ~135°. The same slurry with 20 volume % of HA particles was poured into the Teflon mold. The copper substrate was frozen at a cooling rate of 5°C min^{-1} during observation. Figure 2A shows sequential top-view optical images of the freezing process (movie S1). As also illustrated in Fig. 2B, ice crystals nucleate successively from the hydrophilic to hydrophobic region. They grow preferentially not only in the vertical direction (as is commonly observed in freeze-casting) but also in the horizontal direction perpendicular to the wettability gradient.

Such a unique phenomenon can be attributed to different ice nucleation rates induced by surface wettability. According to the classical nucleation theory (*35*), the heterogeneous nucleation rate (J) of ice can be expressed as

$$J = J_0 \exp(-\Delta G\, k_B^{-1}\, T^{-1}) \quad (1)$$

where J_0 is a proportional constant, k_B is Boltzmann's constant, T is the temperature, and ΔG is the heterogeneous nucleation barrier. In our study, the same freezing conditions were used for all three cases in Fig. 1; thus, the temperature can be considered the same. The only difference was the heterogeneous nucleation barrier (ΔG).

For a flat substrate, the heterogeneous nucleation barrier (ΔG) can be further expressed as (*36*)

$$\Delta G = \Delta G_{homo}(2 - 3m + m^3)/4 \quad (2)$$

where ΔG_{homo} is the homogeneous nucleation barrier. The parameter $m = (\gamma_{sl} - \gamma_{si})/\gamma_{il} \approx \cos\theta^0$ $(-1 < m < 1)$, where θ^0 is the contact angle of the ice nucleus on the substrate, and γ_{sl}, γ_{si}, and γ_{il} are the free energies of substrate-liquid, substrate-ice, and ice-liquid interfaces, respectively.

As the free energy of ice-liquid interface (γ_{il}) can be considered constant for a certain suspension, the parameter m mainly depends on the difference of free energies of the substrate-liquid and substrate-ice

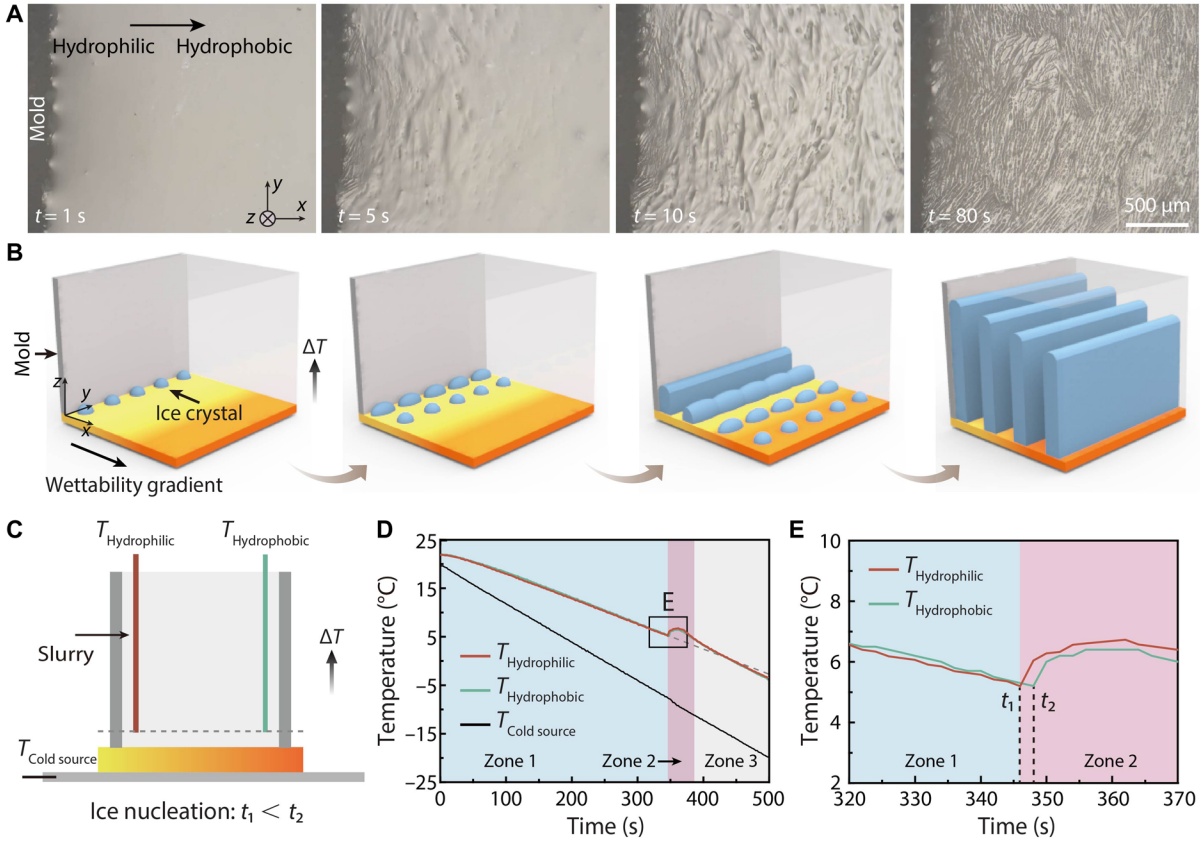

Fig. 2. Observation of the freezing process. (**A**) Top-view optical images showing successive nucleation of ice crystals from the hydrophilic to hydrophobic region and oriented growth perpendicular to the wettability gradient. (**B**) Schematic illustration of the freezing process showing successive nucleation and preferential growth. (**C**) Schematic illustration of thermocouples recording temperature variation above the hydrophilic and hydrophobic regions of the gradient surface. (**D**) Temperature variation of three zones over time. (**E**) Enlarged from (D) showing ice nucleation starts faster on the hydrophilic region.

interfaces ($\gamma_{sl} - \gamma_{si}$), which is determined by the interaction strength of water molecules to the substrate (or the wettability of the substrate) and the lattice match between the ice crystal and the substrate (*36*).

In our study, as we used the same slurry, freezing conditions, and substrate material, the homogeneous nucleation barrier (ΔG_{homo}) and the effect of the lattice match can be considered the same for all three cases in Fig. 1. The only difference was the interaction strength of water molecules to the substrate, i.e., surface wettability. Normally, a hydrophilic surface means a large interaction strength, giving rise to the interfacial free energy differences and thus the parameter m, which further reduces the heterogeneous nucleation barrier (ΔG) and promotes the ice nucleation rate (J) (*37*, *38*). A plot of J as a function of m clearly shows that J increases greatly with m (fig. S6). Therefore, for our surface with a linear wettability gradient, ice crystals nucleate successively from the hydrophilic to hydrophobic region (illustrated in Fig. 2B).

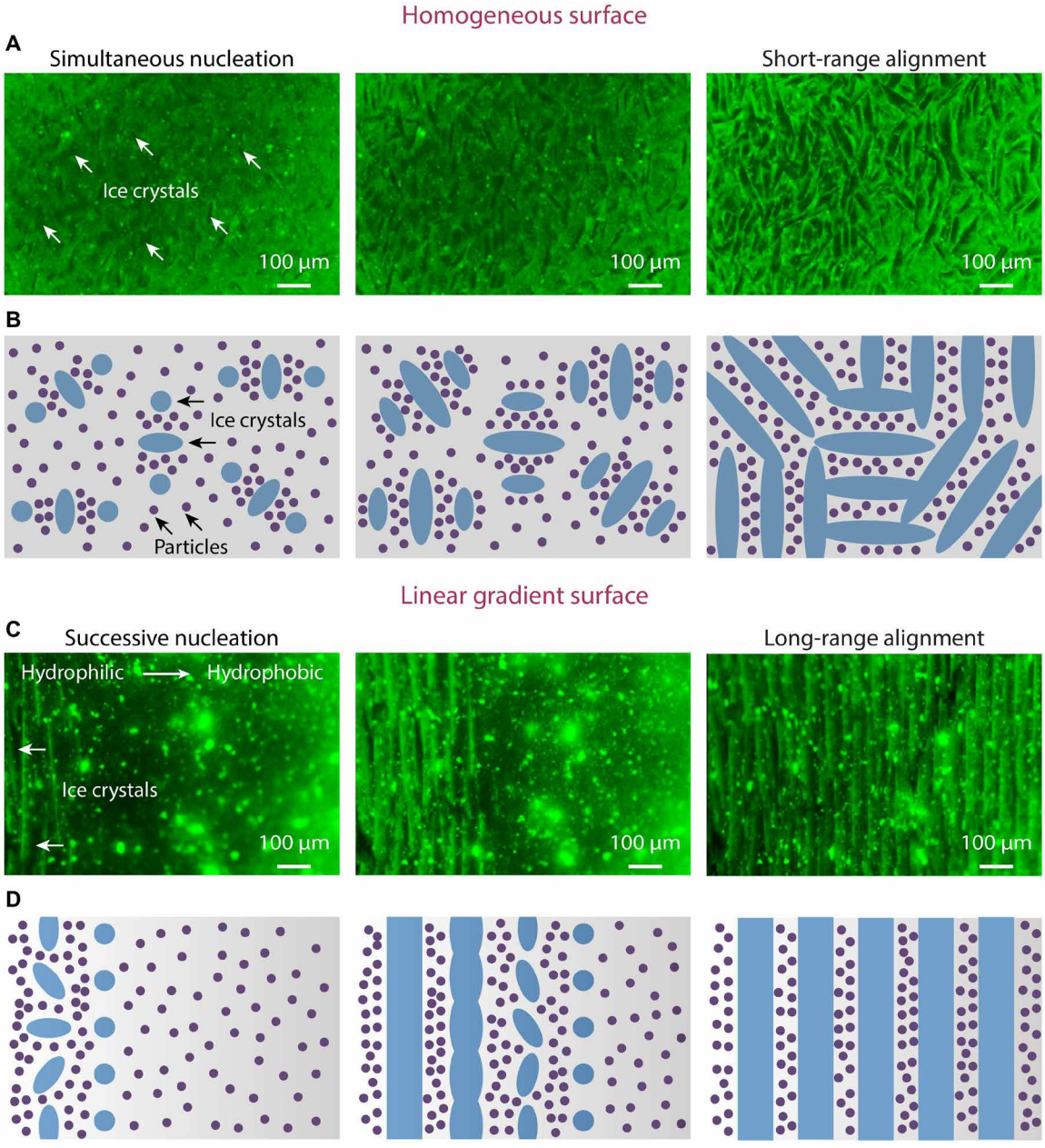

Fig. 3. Proposed freezing mechanism. (**A** and **B**) On a homogeneous surface, the first ice crystals nucleate simultaneously with no favorable location and grow randomly into various orientations. The adjacent crystals grow following their orientations, ultimately forming a multidomain pattern with short-range alignment. (**C** and **D**) On a linear gradient surface, the first ice crystals preferentially nucleate in a row on the most hydrophilic region and expel particles to align perpendicular to the gradient. With these aligned particles forcing the successive ice crystals to grow in a similar orientation, a long-range lamellar structure will be formed. The model (B and D) is proposed on the basis of both theoretical analysis and in situ observation using a fluorescence microscope (A and C). While most of the particles are expelled by the growing ice crystals, a small amount of particles can be trapped in ice. The illustration is simplified to highlight the orientation of the ice crystals.

To further investigate the effect of surface wettability on the ice nucleation rate, we used two thermocouples to record temperature variation above the hydrophilic and hydrophobic regions of the gradient surface, respectively (Fig. 2C). As shown in Fig. 2D, upon freezing, the slurry temperature decreased linearly before ice nucleation (zone 1). The cooling slope is almost identical for both sides, indicating that the impact of surface treatment on the thermal conductivity is negligible. The sudden temperature rise in zone 2 is attributed to the heat release upon nucleation. A closer observation on zone 2 indicates that ice nucleation starts faster on the hydrophilic region (Fig. 2E and fig. S7). In addition, the effects of the wettability gradient, freezing velocity, and particle concentration on the microstructure have been extensively studied (figs. S8 to S10).

Proposed freezing mechanism

On the basis of the above observations and theory, we propose here a possible mechanism for controlling freeze-casted structures by surface wettability. Ice crystals "nucleate successively" from the hydrophilic to the hydrophobic region, resulting in a macroscopically aligned distribution of colloidal particles, which further leads to "preferential growth" of ice crystals under restriction. These two key assumptions were studied both theoretically and experimentally in the literature (*36*, *39*, *40*). In this work, we successfully combine these two mechanisms to realize complex architectures in freeze-casted materials. The freezing processes on the homogeneous and linear gradient surfaces were further observed in situ under a fluorescence microscope (Fig. 3 and movie S2). Here, the same HA slurry was used after mixing with a small amount of fluorescent polystyrene microspheres (1 mg ml^{-1}) for better observation. On a homogeneous surface, the first ice crystals tend to nucleate simultaneously with no favorable location and grow randomly into various orientations. The ellipsoidal shape illustrates the strong growth anisotropy of the ice crystals (*39*). The adjacent crystals will thereafter follow their orientations for unconstrained growth (*39*, *40*) and ultimately form a multidomain pattern with short-range alignment (Fig. 3, A and B). On a linear gradient surface, the first ice crystals preferentially nucleate in a row on the most hydrophilic region. The colloidal particles expelled by such a row of ice crystals are macroscopically aligned perpendicular to the wettability gradient, regardless of the growth orientation of a single nucleus. These aligned particles force the successive ice crystals to grow in a similar orientation, ultimately forming a long-range lamellar structure (Fig. 3, C and D).

Fabrication of the high-performance nacre-mimetic composite

To demonstrate the potential applications of our approach, the HA scaffold with a long-range aligned lamellar structure was further

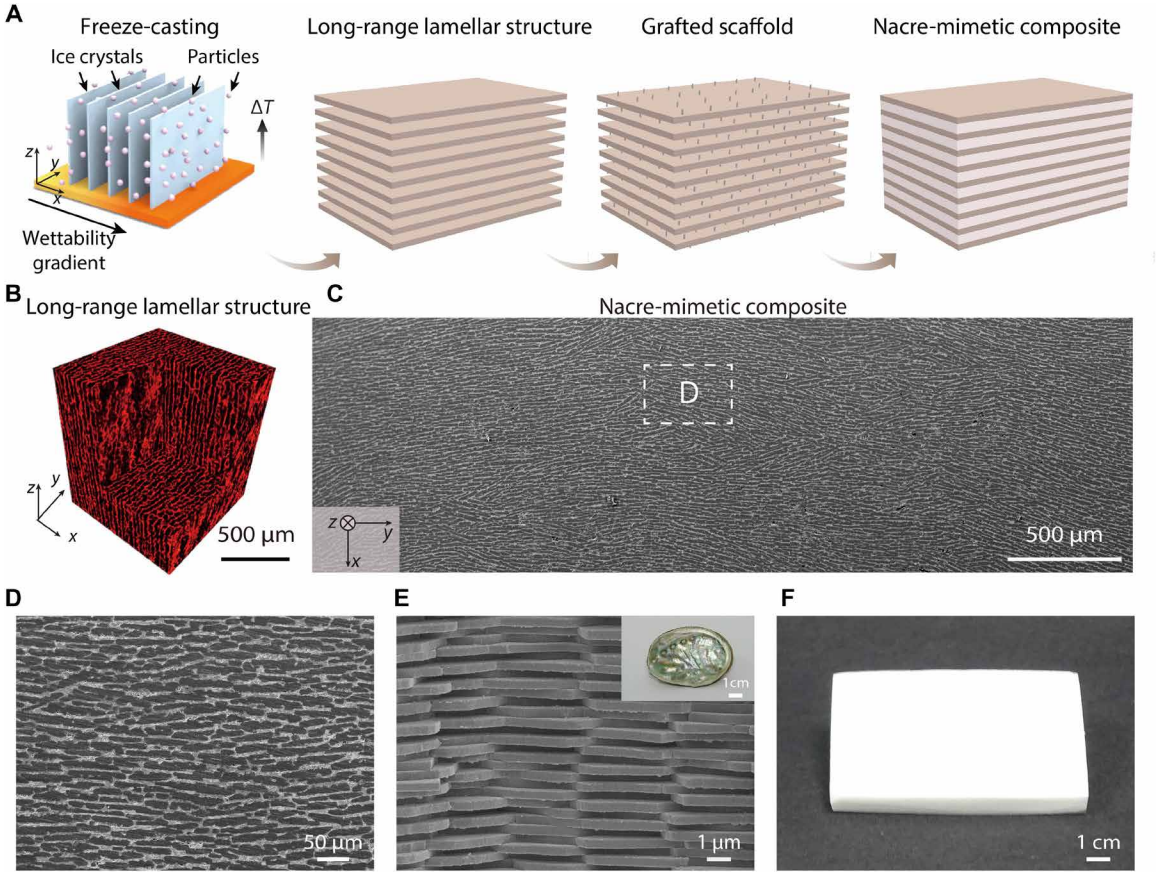

Fig. 4. Fabrication of the nacre-mimetic composite. (**A**) Schematic illustration of the fabrication process. (**B**) Micro–computed tomography image showing a long-range lamellar structure throughout the observed area. (**C**) SEM image showing the long-range lamellar structure remained after compounding with PMMA. (**D**) Enlarged SEM image showing the detailed lamellar structure similar to that of natural nacre (**E**). (**F**) Optical image showing a large piece of bulk nacre-mimetic HA/PMMA composite (roughly 10 cm by 8 cm by 1 cm), reflecting the scalability of our approach. Photo credit: Nifang Zhao, Zhejiang University.

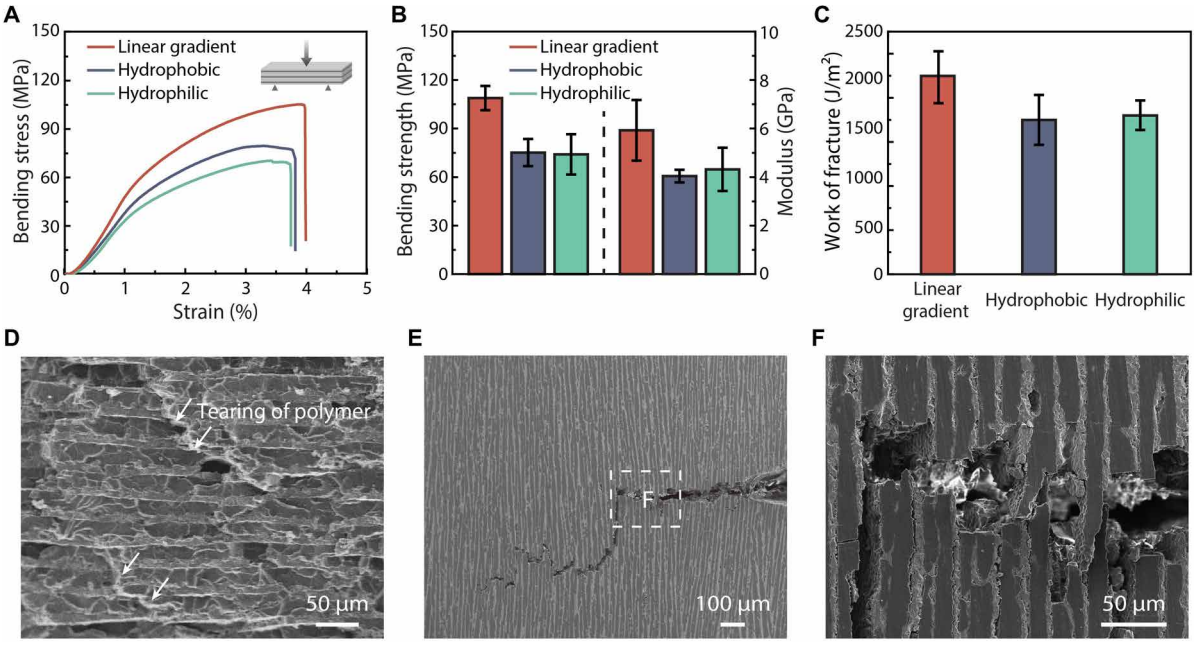

Fig. 5. Mechanical properties of the nacre-mimetic composite. (**A**) Three-point bending curves of the HA/PMMA composites prepared with the three types of surfaces. (**B** and **C**) The bending strength, Young's modulus, and work of fracture of the nacre-mimetic composite are better than those prepared with homogeneously hydrophilic and hydrophobic surfaces. (**D** to **F**) SEM images showing that the nacre-mimetic composite shares the same toughening mechanism with natural nacre. (D) Fracture surface showing the tearing of the PMMA layers. (E) Under the single-edge notched bending test, the crack initiates from the notch and propagates along a tortuous path. (F) Enlarged SEM image of (E) showing interface failure, crack bridging, and ceramic pull-out.

sintered and compounded with polymer [polymethyl methacrylate (PMMA)] to generate a high-performance nacre-mimetic composite, following the fabrication process in Fig. 4A. The well-oriented structure (as confirmed by a micro–computed tomography image, shown in Fig. 4B) is reserved after polymer infiltration (Fig. 4, C and D), mimicking the brick-and-mortar structure of natural nacre (Fig. 4E). The large sample in Fig. 4F (around 10 cm by 8 cm by 1 cm) demonstrates the scalability of our current approach (fig. S11). Ideally, the in-plane (*xy* plane) size of the sample is only limited by the size of the cooling stage. The height of the *z* axis is limited by a stable cooling velocity. Note that particle sedimentation may affect the homogeneity of the freeze-casted structure. In this work, as the sedimentation velocity of HA particles is very low (estimated as ~0.56 μm s^{-1}; Supplementary Discussions), no obvious inhomogeneity in the horizontal direction caused by successive ice nucleation is observed. When freezing for a relatively long time for large samples, inhomogeneity in the vertical direction induced by sedimentation needs to be considered. To obtain large size samples with uniform structure, both the particle concentration and ice growth velocity should remain unchanged during the whole freezing process.

Mechanical properties of the nacre-mimetic composite

To show the impact of the resulting structure on the mechanical properties, we compared the flexural properties of the HA/PMMA composites fabricated by freeze-casting on gradient and homogeneous surfaces (Fig. 5A). The bending strength, modulus, and work of fracture of the nacre-mimetic composites are 108.9 ± 7.5 MPa, 5.93 ± 1.25 GPa, and 2232 ± 295 J/m^2, respectively, superior to those prepared on homogeneously hydrophobic (75.1 ± 8.4 MPa, 4.04 ± 0.26 GPa, and 1749 ± 283 J/m^2) and hydrophilic (74.0 ± 12.4 MPa, 4.31 ± 0.89 GPa, and 1802 ± 168 J/m^2) surfaces (Fig. 5, B and C, fig. S12, and table S1). The substantial improvement in mechanical properties of the nacre-mimetic composite clearly shows the advantage of the long-range lamellar structure. During loading, the stretching and bridging of the PMMA layers contribute to the toughening mechanism of the composite, as demonstrated by the tearing of the PMMA layers after fracture (Fig. 5D). The single-edge notched bending test was performed to further analyze the function of the long-range lamellar structure. As shown in Fig. 5 (E and F), the crack initiates from the notch and propagates along a tortuous path, accompanied by interface failure, crack bridging, and ceramic "pull-out," which is consistent with the toughening mechanism of the natural nacre (*1*). These results further demonstrate that freeze-casting on a gradient surface is an effective approach to fabricate high-performance nacre-mimetic composites.

Designability of surface wettability pattern

To further demonstrate the potential of our strategy, we performed freeze-casting on copper surfaces with both bilayer linear wettability gradient and radial wettability gradient (fig. S13). Correspondingly, two representative structures with cross-aligned (Fig. 6A) and circular (Fig. 6, C to F) lamellar patterns can be obtained, which are impossible to realize with conventional freeze-casting techniques. The mechanical properties of these composites were thoroughly investigated by three-point bending and compression (fig. S12 and table S1). We emphasized bending or compression properties of our materials based on their potential applications. For example, the single-aligned and cross-aligned lamellar structures are aimed at mimicking the structures of nacre and abalone shell, which are mainly loaded under bending (*5*). The circular lamellar structure is designed to mimic the structure of the cortical bone where compression is more critical (*1*). Specifically, the bilayer composite with a cross-aligned lamellar structure,

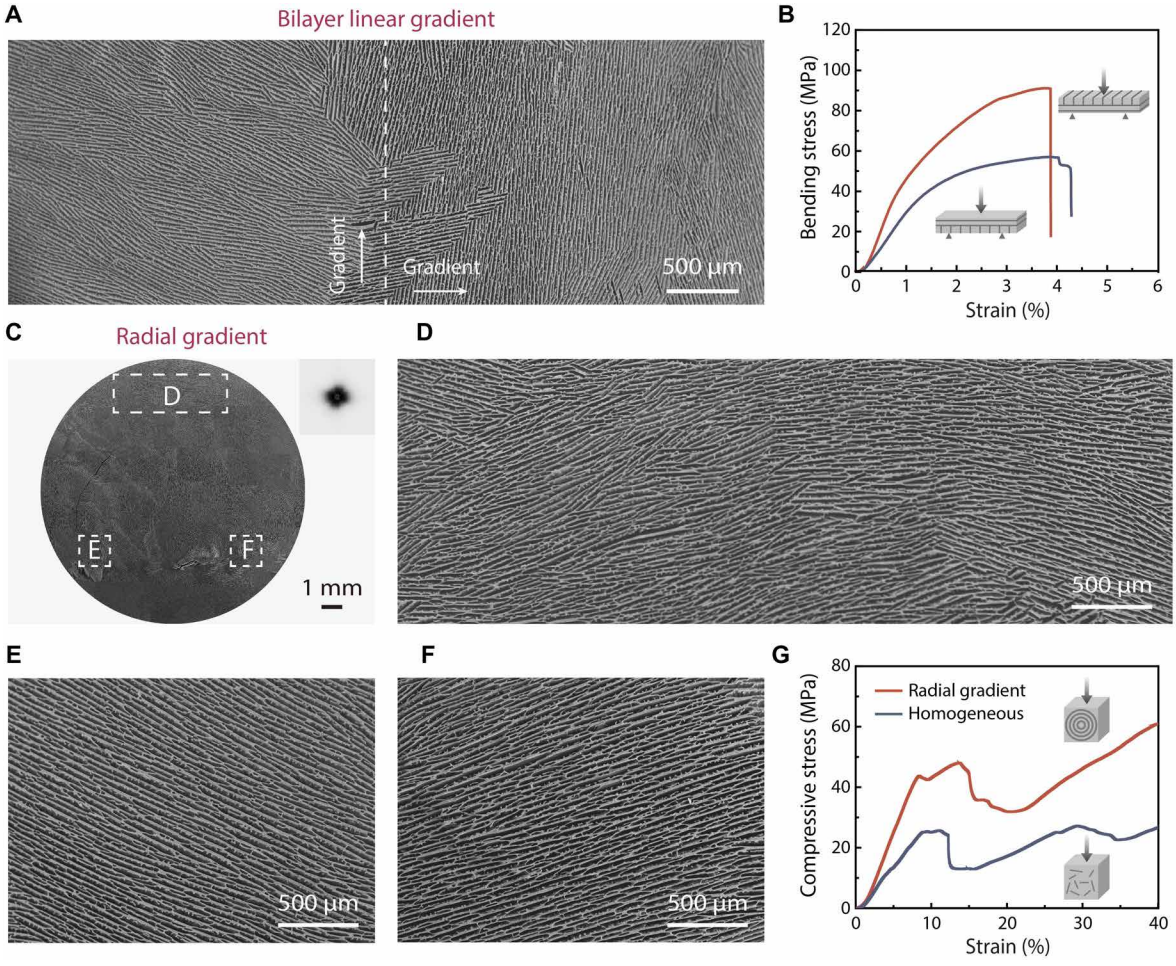

Fig. 6. Designability of the surface wettability pattern. (**A**) SEM image of the cross section parallel to the cold substrate, showing a cross-aligned lamellar structure. (**B**) Three-point bending curves of the HA/PMMA composites showing high anisotropy. (**C**) SEM image of the cross section parallel to the cold substrate, showing a circular long-range lamellar structure orients perpendicular to the wettability gradient. The orientation analysis by software ImageJ confirms the circular structure. (**D** to **F**) Enlarged SEM images from three regions showing the lamellar structure with different orientations guided by the wettability gradient. (**G**) Compression curves of the HA/PMMA composites with circular and multidomain lamellar structures prepared with radial gradient and homogeneous surfaces, respectively.

mimicking abalone shell (*5*), shows drastically different flexural strength and modulus, depending on the lamellar alignment in the upper layer (out-of-plane: 90.3 ± 4.0 MPa and 5.88 ± 1.39 GPa; in-plane: 60.1 ± 7.4 MPa and 3.44 ± 0.64 GPa; Fig. 6B). The composite with a circular lamellar structure, mimicking cortical bone (*1*), shows higher compressive strength and modulus than that with a multidomain lamellar structure (circular: 46.1 ± 2.1 MPa and 0.59 ± 0.09 GPa; multidomain: 25.7 ± 2.1 MPa and 0.43 ± 0.05 GPa; Fig. 6G). These results further confirm the possibility of harnessing the rich designability of surface wettability patterns to make high-performance bulk materials with complex bioinspired architectures.

CONCLUSION

In conclusion, we demonstrate that ice nucleation and growth can be controlled by introducing a wettability gradient onto the cold surface. The wettability gradient yields successive ice nucleation and preferential ice growth, which act synergistically to control the orientation of the ice crystals and the architecture of the resulting porous material. As a proof of concept, we demonstrate that a long-range aligned lamellar structure (>10 cm, limited only by size of the cooling stage) can be obtained by freeze-casting on a surface with a linear wettability gradient. Subsequent infiltration of this porous scaffold generates a high-performance bulk nacre-mimetic composite with excellent strength and toughness. In addition, cross-aligned and circular lamellar structures can be obtained by freeze-casting on surfaces modified with bilayer linear wettability gradient and radial wettability gradient, respectively, which are impossible to realize with conventional freeze-casting techniques. Our study highlights the potential of harnessing the rich designability of surface wettability patterns to build bioinspired materials with complex architectures and high performance.

MATERIALS AND METHODS

Materials

The copper substrate (20 mm by 20 mm by 1 mm), microscope cover glass (18 mm by 18 mm by 0.15 mm), and abrasive papers (800#, 1000#, 3000#, and 7000#) were purchased from a local store. Ethanol (AR) and hydrogen peroxide (30%, AR) were purchased from Sinopharm Chemistry Co. Ltd., China. POTS and poly(ethylene glycol) (PEG-300)

were bought from Sigma-Aldrich Chemistry Co. Ltd., USA. The HA powders [density = 3.15 g cm^{-3}, *d*50 (median particle) size = 2.424 μm] were purchased from Trans-Tech, Adamstown, MD, USA. Darvan 811 was purchased from R.T. Vanderbilt Co., Norwalk, CT, USA. The Aquazol polymer with a molecular weight of 50,000 g mol^{-1} was purchased from Polymer Chemistry Innovations Inc., Tucson, USA. 3-(trimethoxysilyl)propyl methacrylate (γ-MPS) was purchased from Shanghai Macklin Biochemical Co. Ltd., China. 2,2-Azodiisobutyronitrile (AIBN) and methyl methacrylate (MMA) were purchased from Aladdin Chemistry Co. Ltd., China. Waterborne polyurethane (PU-3777A) was purchased from ShunDe SanSheng Trade Co. Ltd., China. Green fluorescent polystyrene microspheres (diameter, around 1 μm; excitation peak, 488 nm; emission peak, 518 nm) were purchased from Tianjin Unibead Scientific Co. Ltd., China.

Fabrication of the homogeneously hydrophilic copper surface

The copper substrate was first polished by abrasive papers (800#, 1000#, 3000#, and 7000#, successively) and then cleaned by ultrasonic stirring in an ethanol bath for 10 min. After being rinsed with deionized water, the copper substrate was immersed in 30% hydrogen peroxide with ultrasonic washing for 20 min. Last, after being rinsed with deionized water and ethanol, the copper substrate was dried with inert gas.

Fabrication of the homogeneously hydrophobic copper surface

The treated hydrophilic copper substrate was put in a desiccator with a drop of POTS (5 μl) to allow effective surface modification under POTS atmosphere for an hour. After being rinsed with ethanol, the modified surface became hydrophobic.

Fabrication of the copper surface with linear wettability gradients

A drop of POTS (2 μl) and a cup of deionized water were put in an airtight container. Then, the hydrophilic copper substrate was fixed on strings by a clamp (see the schematic illustration in fig. S1E). After that, the copper substrate was slowly dipped into the deionized water in the airtight container until it was totally immersed at a constant speed. This exposed the copper substrate to the POTS atmosphere for different lengths of time, generating a wettability gradient on the copper substrate along the dipping direction. The dipping down speed was about 0.3 mm min^{-1}, depending on the modification area required on the substrate. The copper substrate was lastly rinsed with ethanol and dried with inert gas. The copper surface with a bilayer linear gradient was fabricated by combining two substrates with linear gradient.

Fabrication of the copper surface with a radial wettability gradient

A drop of POTS (0.5 μl, 1 volume % POTS in ethanol) was added in the center of the hydrophilic copper substrate (~20°). The copper substrate was put in the fume hood to allow ethanol evaporation and successful surface modification. After 2 hours, a radial wettability gradient was introduced with the water contact angle increasing from the edge (~60°) to the center (~135°).

Fabrication of the three-dimensional porous scaffold

Square Teflon tubes were sealed on the copper substrates with different wettability. A slurry was prepared by mixing distilled water with HA powders (20 volume %), Darvan 811 as dispersant (1 wt %), poly(ethylene glycol) as lubricant (1 wt %), and Aquazol as binder (2 wt %). The slurry was ball-milled for at least 24 hours and degassed before freezing. The slurry was poured into the mold and frozen on the copper substrates with different wettability at a cooling rate of 5°C min^{-1}. After being entirely frozen, the sample was tapped out of the mold and freeze-dried for more than 24 hours at −60°C with a freeze dryer under a pressure of 0.05 mbar (Labconco 8811, Kansas City, USA). The freeze-dried sample was sintered at 1300°C for 4 hours.

In situ observation of the freezing process

The setup is illustrated in fig. S5. A Teflon mold (12 mm by 12 mm by 1 mm) was sealed to the copper substrate with a linear wettability gradient from ~20° to ~135°. When observing under an optical microscope, the slurry with 20 volume % of HA particles was poured into the Teflon mold. The copper substrate was frozen at a cooling rate of 5°C min^{-1} during observation. When observing under a fluorescence microscope, the same slurry mixed with green fluorescent polystyrene microspheres (1 mg ml^{-1}) was used. The copper substrate was frozen at a cooling rate of 2°C min^{-1} to generate a proper ice growth velocity for better observation.

Fabrication of nacre-mimetic composites

The as-prepared HA scaffold was immersed into 1 wt % γ-MPS/ethanol solution for 24 hours and modified with γ-MPS. After being dried at 80°C for 2 hours, the scaffold was infiltrated in a mixture of MMA and initiator AIBN (0.5 wt %) at 40°C for in situ polymerization. After 3 days, the composite was treated at 90°C for another 2 hours to guarantee full polymerization.

Characterization

The contact angle was measured by an optical contact angle meter (OCA 50, Dataphysics, Germany) with water droplets (2 μl) at ambient temperature. SEM images were gathered by Hitachi S-3500N at an acceleration voltage of 5 kV. Three-point bending of unnotched samples with a loading span of 16 mm was tested using an Instron 5944 testing system (USA) at a displacement rate of 0.015 mm s^{-1}. All samples were cut and polished into beams of around 4 mm by 3 mm by 30 mm. At least five samples were tested to obtain statistically reliable values. To examine the path of the crack until failure, single-edge notched beams were fabricated using a low-speed saw to a depth of ~1.5 mm, with the notch root sharpened with a razor blade. The single-edge notched beams were tested in three-point bending at a displacement rate of 1 μm s^{-1}, with a loading span of 16 mm. The compression properties were tested using a Zwick/Roell Z020 (Germany) at a displacement rate of 1 mm min^{-1}. All samples were cut and polished into blocks of roughly 10 mm by 10 mm by 10 mm. At least five samples were tested to obtain statistically reliable values. The x-ray micro–computed tomography was tested by a Zeiss/Xradia 520 Versa, Germany.

SUPPLEMENTARY MATERIALS

Supplementary material for this article is available at http://advances.sciencemag.org/cgi/content/full/6/31/eabb4712/DC1

REFERENCES AND NOTES

1. U. G. K. Wegst, H. Bai, E. Saiz, A. P. Tomsia, R. O. Ritchie, Bioinspired structural materials. *Nat. Mater.* **14**, 23–36 (2015).

2. Z. Liu, M. A. Meyers, Z. Zhang, R. O. Ritchie, Functional gradients and heterogeneities in biological materials: Design principles, functions, and bioinspired applications. *Prog. Mater. Sci.* **88**, 467–498 (2017).
3. A. R. Studart, Additive manufacturing of biologically-inspired materials. *Chem. Soc. Rev.* **45**, 359–376 (2016).
4. M. Eder, S. Amini, P. Fratzl, Biological composites-complex structures for functional diversity. *Science* **362**, 543–547 (2018).
5. A. Lin, M. A. Meyers, Growth and structure in abalone shell. *Mat. Sci. Eng. A Struct.* **390**, 27–41 (2005).
6. J. Wang, Q. Cheng, Z. Tang, Layered nanocomposites inspired by the structure and mechanical properties of nacre. *Chem. Soc. Rev.* **41**, 1111–1129 (2012).
7. K. Chen, B. Shi, Y. Yue, J. Qi, L. Guo, Binary synergy strengthening and toughening of bio-inspired nacre-like graphene oxide/sodium alginate composite paper. *ACS Nano* **9**, 8165–8175 (2015).
8. B. Yeom, T. Sain, N. Lacevic, D. Bukharina, S.-H. Cha, A. M. Waas, E. M. Arruda, N. A. Kotov, Abiotic tooth enamel. *Nature* **543**, 95–98 (2017).
9. T. Guo, L. Heng, M. Wang, J. Wang, L. Jiang, Robust underwater oil-repellent material inspired by columnar nacre. *Adv. Mater.* **28**, 8505–8510 (2016).
10. X. Meng, M. Wang, L. Heng, L. Jiang, Underwater mechanically robust oil-repellent materials: Combining conflicting properties using a heterostructure. *Adv. Mater.* **30**, 1706634 (2018).
11. S. Deville, E. Saiz, R. K. Nalla, A. P. Tomsia, Freezing as a path to build complex composites. *Science* **311**, 515–518 (2006).
12. E. Munch, M. E. Launey, D. H. Alsem, E. Saiz, A. P. Tomsia, R. O. Ritchie, Tough, bio-inspired hybrid materials. *Science* **322**, 1516–1520 (2008).
13. Q. Cheng, C. Huang, A. P. Tomsia, Freeze casting for assembling bioinspired structural materials. *Adv. Mater.* **29**, 1703155 (2017).
14. L.-B. Mao, H.-L. Gao, H.-B. Yao, L. Liu, H. Cölfen, G. Liu, S.-M. Chen, S.-K. Li, Y.-X. Yan, Y.-Y. Liu, S.-H. Yu, Synthetic nacre by predesigned matrix-directed mineralization. *Science* **354**, 107–110 (2016).
15. R. P. Wilkerson, B. Gludovatz, J. Watts, A. P. Tomsia, G. E. Hilmas, R. O. Ritchie, A novel approach to developing biomimetic ("nacre-like") metal-compliant-phase (nickel-alumina) ceramics through coextrusion. *Adv. Mater.* **28**, 10061–10067 (2016).
16. Y. Yang, X. Li, M. Chu, H. Sun, J. Jin, K. Yu, Q. Wang, Q. Zhou, Y. Chen, Electrically assisted 3D printing of nacre-inspired structures with self-sensing capability. *Sci. Adv.* **5**, eaau9490 (2019).
17. G. Du, A. Mao, J. Yu, J. Hou, N. Zhao, J. Han, Q. Zhao, W. Gao, T. Xie, H. Bai, Nacre-mimetic composite with intrinsic self-healing and shape-programming capability. *Nat. Commun.* **10**, 800 (2019).
18. C. Ferraro, E. Garcia-Tuñon, V. G. Rocha, S. Barg, M. D. Fariñas, T. E. Gomez Alvarez-Arenas, G. Sernicola, F. Giuliani, E. Saiz, Light and strong SiC networks. *Adv. Funct. Mater.* **26**, 1636–1645 (2016).
19. Z.-L. Yu, N. Yang, L.-C. Zhou, Z.-Y. Ma, Y.-B. Zhu, Y.-Y. Lu, B. Qin, W.-Y. Xing, T. Ma, S.-C. Li, H.-L. Gao, H.-A. Wu, S.-H. Yu, Bioinspired polymeric woods. *Sci. Adv.* **4**, eaat7223 (2018).
20. Z. Zeng, H. Jin, M. Chen, W. Li, L. Zhou, Z. Zhang, Lightweight and anisotropic porous MWCNT/WPU composites for ultrahigh performance electromagnetic interference shielding. *Adv. Funct. Mater.* **26**, 303–310 (2016).
21. N. Zhao, M. Yang, Q. Zhao, W. Gao, T. Xie, H. Bai, Superstretchable nacre-mimetic graphene/poly(vinyl alcohol) composite film based on interfacial architectural engineering. *ACS Nano* **11**, 4777–4784 (2017).
22. J. Han, G. Du, W. Gao, H. Bai, An anisotropically high thermal conductive boron nitride/epoxy composite based on nacre-mimetic 3D network. *Adv. Funct. Mater.* **29**, 1900412 (2019).
23. H. Bai, Y. Chen, B. Delattre, A. P. Tomsia, R. O. Ritchie, Bioinspired large-scale aligned porous materials assembled with dual temperature gradients. *Sci. Adv.* **1**, e1500849 (2015).
24. H. Bai, F. Walsh, B. Gludovatz, B. Delattre, C. Huang, Y. Chen, A. P. Tomsia, R. O. Ritchie, Bioinspired hydroxyapatite/poly(methyl methacrylate) composite with a nacre-mimetic architecture by a bidirectional freezing method. *Adv. Mater.* **28**, 50–56 (2016).
25. C. Wang, X. Chen, B. Wang, M. Huang, B. Wang, Y. Jiang, R. S. Ruoff, Freeze-casting produces a graphene oxide aerogel with a radial and centrosymmetric structure. *ACS Nano* **12**, 5816–5825 (2018).
26. E. Munch, E. Saiz, A. P. Tomsia, S. Deville, Architectural control of freeze-cast ceramics through additives and templating. *J. Am. Ceram. Soc.* **92**, 1534–1539 (2009).
27. S. Deville, Ice-templating, freeze casting: Beyond materials processing. *J. Mater. Res.* **28**, 2202–2219 (2013).
28. M. M. Porter, M. Yeh, J. Strawson, T. Goehring, S. Lujan, P. Siripasopsotorn, M. A. Meyers, J. McKittrick, Magnetic freeze casting inspired by nature. *Mater. Sci. Eng. A* **556**, 741–750 (2012).
29. P. Niksiar, M. B. Frank, J. McKittrick, M. M. Porter, Microstructural evolution of paramagnetic materials by magnetic freeze casting. *J. Mater. Res. Technol.* **8**, 2247–2254 (2019).
30. S. Wu, C. Zhu, Z. He, H. Xue, Q. Fan, Y. Song, J. S. Francisco, X. C. Zeng, J. Wang, Ion-specific ice recrystallization provides a facile approach for the fabrication of porous materials. *Nat. Commun.* **8**, 15154 (2017).
31. M. J. Kreder, J. Alvarenga, P. Kim, J. Aizenberg, Design of anti-icing surfaces: Smooth, textured or slippery? *Nat. Rev. Mater.* **1**, 15003 (2016).
32. J. Lv, Y. Song, L. Jiang, J. Wang, Bio-inspired strategies for anti-icing. *ACS Nano* **8**, 3152–3169 (2014).
33. H.-L. Gao, Y.-B. Zhu, L.-B. Mao, F.-C. Wang, X.-S. Luo, Y.-Y. Liu, Y. Lu, Z. Pan, J. Ge, W. Shen, Y.-R. Zheng, L. Xu, L.-J. Wang, W.-H. Xu, H.-A. Wu, S.-H. Yu, Super-elastic and fatigue resistant carbon material with lamellar multi-arch microstructure. *Nat. Commun.* **7**, 12920 (2016).
34. F. Bouville, E. Portuguez, Y. Chang, G. L. Messing, A. J. Stevenson, E. Maire, L. Courtois, S. Deville, Templated grain growth in macroporous materials. *J. Am. Ceram. Soc.* **97**, 1736–1742 (2014).
35. J. Frenkel, A general theory of heterophase fluctuations and pretransition phenomena. *J. Chem. Phys.* **7**, 538–547 (1939).
36. Z. Zhang, X.-Y. Liu, Control of ice nucleation: Freezing and antifreeze strategies. *Chem. Soc. Rev.* **47**, 7116–7139 (2018).
37. L. Lupi, V. Molinero, Does hydrophilicity of carbon particles improve their ice nucleation ability? *J. Phys. Chem. A* **118**, 7330–7337 (2014).
38. M. Fitzner, G. C. Sosso, S. J. Cox, A. Michaelides, The many faces of heterogeneous ice nucleation: Interplay between surface morphology and hydrophobicity. *J. Am. Chem. Soc.* **137**, 13658–13669 (2015).
39. S. Deville, E. Maire, A. Lasalle, A. Bogner, C. Gauthier, J. Leloup, C. Guizard, In situ x-ray radiography and tomography observations of the solidification of aqueous alumina particle suspensions. Part II: Steady state. *J. Am. Ceram. Soc.* **92**, 2497–2503 (2009).
40. S. Deville, *Freezing Colloids: Observations, Principles, Control, and Use* (Springer, 2017).

Acknowledgments: We are grateful for N. Zheng for assistance on SEM images. **Funding:** This work was supported by the National Natural Science Foundation of China (grant nos. 51722306, 51603182, and 21674098), the National Key Research and Development Program of China (2017YFC1103900), and the Fundamental Research Funds for the Central Universities (no. 2018XZZX002-15). **Author contributions:** H.B. conceived the concept and supervised the project. N.Z., M.L., and H.G. performed the experiments. Experimental results were analyzed through contributions of all authors. H.B. and N.Z. wrote the manuscript. **Competing interests:** The authors declare that they have no competing interests. **Data and materials availability:** All data needed to evaluate the conclusions in the paper are present in the paper and/or the Supplementary Materials. Additional data related to this paper may be requested from the authors.

Submitted 26 February 2020
Accepted 15 June 2020
Published 31 July 2020
10.1126/sciadv.abb4712

Citation: N. Zhao, M. Li, H. Gong, H. Bai, Controlling ice formation on gradient wettability surface for high-performance bioinspired materials. *Sci. Adv.* **6**, eabb4712 (2020).